ARL-TR-7318 ● JUNE 2015

US Army Research Laboratory

Effect of Carbon Doping on the Electronic Structure and Elastic Properties of Boron Suboxide

by Amol B Rahane, Jennifer S Dunn, and Vijay Kumar

NOTICES

Disclaimers

The findings in this report are not to be construed as an official Department of the Army position unless so designated by other authorized documents.

Citation of manufacturer's or trade names does not constitute an official endorsement or approval of the use thereof.

Destroy this report when it is no longer needed. Do not return it to the originator.

ARL-TR-7318 ● JUNE 2015

US Army Research Laboratory

Effect of Carbon Doping on the Electronic Structure and Elastic Properties of Boron Suboxide

by Amol B Rahane and Vijay Kumar
Dr Vijay Kumar Foundation, Haryana, India

Jennifer S Dunn
Weapons and Materials Research Directorate, ARL

REPORT DOCUMENTATION PAGE

Form Approved
OMB No. 0704-0188

1. REPORT DATE *(DD-MM-YYYY)*	2. REPORT TYPE	3. DATES COVERED (From - To)
June 2015	Final	1 October 2013–1 September 2014

4. TITLE AND SUBTITLE
Effect of Carbon Doping on the Electronic Structure and Elastic Properties of Boron Suboxide

5a. CONTRACT NUMBER

5b. GRANT NUMBER

5c. PROGRAM ELEMENT NUMBER

6. AUTHOR(S)
Amol B Rahane, Jennifer S Dunn, and Vijay Kumar

5d. PROJECT NUMBER
TA-RA1

5e. TASK NUMBER

5f. WORK UNIT NUMBER

7. PERFORMING ORGANIZATION NAME(S) AND ADDRESS(ES)
US Army Research Laboratory
ATTN: RDRL-WMM-E
Aberdeen Proving Ground, MD 21085-5069

8. PERFORMING ORGANIZATION REPORT NUMBER
ARL-TR-7318

9. SPONSORING/MONITORING AGENCY NAME(S) AND ADDRESS(ES)

10. SPONSOR/MONITOR'S ACRONYM(S)

11. SPONSOR/MONITOR'S REPORT NUMBER(S)

12. DISTRIBUTION/AVAILABILITY STATEMENT
Approved for public release distribution unlimited.

13. SUPPLEMENTARY NOTES

14. ABSTRACT

In this report, we use density functional theory to determine the effect of carbon (C) contamination on the electronic structure and elastic properties of boron suboxide (B_6O. The electron localization surface identified 3 distinct bonding regions: 1) short, highly covalent, B_p - B_p bonds connecting 2 icosahedra; 2) ionic bonding between the equatorial boron (B) and oxygen (O); and 3) intra-icosahedral boron (B_p- B_e) bonding. When C is doped at an oxygen site, the sp^2 hybridized carbon forms bonds with 3 neighboring equatorial B_e atoms, and the elastic moduli decrease between 0.4% and 1.7%. If 2 carbon atoms are doped at 2 neighboring oxygen sites, both carbon atoms become sp^2 hybridized and the bulk modulus increases by 0.3%, yet the shear and Young's modulus decrease by 0.5%. When an interstitial atom is placed between these 2 carbons, forming C-B-C or C-C-C chains, the terminal carbons become tetrahedrally "sp^3 like" bonded. By promoting the formation of a local B_4C-like structure, it may be possible to improve the mechanical stability and elastic properties of B_6O.

15. SUBJECT TERMS
B_6O, DFT, elastic properties, ELF, carbon

16. SECURITY CLASSIFICATION OF:			17. LIMITATION OF ABSTRACT	18. NUMBER OF PAGES	19a. NAME OF RESPONSIBLE PERSON
					Amol B Rahane
a. REPORT	b. ABSTRACT	c. THIS PAGE			19b. TELEPHONE NUMBER (Include area code)
Unclassified	Unclassified	Unclassified	UU	38	410-306-0750

Contents

List of Figures

List of Tables

Acknowledgments

We acknowledge the Center for Development of Advance Computing, Pune, for providing the supercomputing facilities and the US Army Research Laboratory for funding this research.

1. Introduction

Boron suboxide (B_6O) is a promising material system for lightweight armor applications. It has an ultra-high hardness[1,2] (24–45 GPa), low density (~2.61 g/cc), high mechanical strength (26–30 GPa),[3] high oxidation resistance[4] (below 1,200 °C), and is chemically inert. However, it has yet to be fielded in Soldier-mounted protection due to several processing and performance-based challenges including: 1) trans-granular failure resulting in low fracture toughness,[5,6] 2) a reduction in shear strength under extreme environmental conditions[7,8] such as high temperature and pressure, and 3) manufacturing challenges (i.e., narrow processing window, high pressure) required to create highly crystalline, fully dense stoichiometric B_6O.[9] To maximize the performance of B_6O as a lightweight armor material, we must first understand the competing influences of crystal structure, defect populations (i.e., vacancies, twins, stacking faults, carbon [C] contamination), stoichiometry, and surface reconstructions on the nature of the atomic bonding within the bulk crystal and near interfaces (i.e., grain/phase boundaries, free surfaces) and associate these effects with specific failure mechanisms (i.e., grain boundary decohesion, twinning/stacking fault formation, intragranular fracture, and bulk/grain boundary amorphization).

B_6O is particularly sensitive to carbon contamination, which can be introduced during any ceramic processing stage (for example, residual organics during powder synthesis due to precursors and ceramic binders, carbon-based mixing media, CO-containing atmosphere during calcination and sintering, graphite sintering sleeves and furnace components, and mechanical treatments such as machining and polishing). Our previous computational study[10] has shown that carbon is highly stable in B_6O. The precipitation of B_4C-like structure within the B_6O unit cell is exothermic, and the energy released increases as more carbon substitutes into the lattice. However, to date a complete understanding of the influence of C contamination on the electronic structure and mechanical properties of B_6O is lacking. In this report, we explore these relationships by studying the effect of stoichiometry and C contamination on the nature of atomic bonding (via electron localization function), the electronic structure, and the mechanical properties (i.e., elastic stiffness tensor, bulk modulus, Young modulus, and shear modulus) of bulk B_6O.

2. Computational Details

First principles density functional theory calculations using the generalized gradient approximation (GGA) given by Perdew-Bruke-Ernzerhof[11] and the

projector augmented wave (PAW) method[12–14] were performed within the Vienna Ab initio Simulation Package (VASP).[15] The plane wave cut-off energy was set to 500 eV. The calculations were considered converged when the maximum force on each ion was less than 0.001 eV/Å, and the change in total energy was less than 10^{-4} eV. The simulation cell consisted of a 42-atom B_6O unit cell in hexagonal representation that was sampled with a 2 × 2 × 1 K-points Monkhorst-Pack grid to obtain structural properties. We performed a full relaxation of the volume, lattice parameters, and all internal atomic coordinates. The calculated equilibrium lattice parameters for B_6O unit cell are a = 5.393 Å and c = 12.327 Å, which are in good agreement with the experimental values of Higashi[16] (a = 5.374 Å and c = 12.331 Å) and Hubert[17] (a = 5.3902 Å and c = 12.3125 Å, c/a ratio = 2.284). Hubert's B_6O was oxygen (O) deficient (maximum achieved O occupancy = 0.95 at 6 GPa). Therefore, when extrapolated to ideal stoichiometry, Hubert's lattice parameters are a = 5.399 Å and c = 12.306 Å. Calculations that considered the effect of carbon doping required a larger 2 × 2 × 1 supercell (168 atoms) to prevent the artificial interaction between defect states across the periodic boundary. The lattice parameters calculated at the Γ-point (a = 5.396 Å and c = 12.311 Å) are similar to the 3 × 3 × 3 k-points calculations (a = 5.394 Å and c = 12.318 Å). Therefore, Γ-point calculations were used to study the doped system.

3. Results and Discussion

3.1 Structural and Electronic Properties

To understand how carbon contamination affects the bonding character and electronic structure of B_6O, we performed a detailed analysis of the total density of states (DOS), charge density distribution, and corresponding electron localization function (ELF). The ELF is defined by Becke and Edgecombe[18] as the probability density for finding a second like-spin electron near a reference point. ELF is a dimensionless relative measure of the electron localization, which is calibrated with respect to a probability density for a uniform electron gas. High ELF values (ELF ~ 1) indicate that the electrons are more localized than in a uniform electron gas of the same density. It is possible to differentiate between ionic, covalent, and metallic bonding from a qualitative analysis of the ELF map. Covalent bonding is indicated by a maxima in the ELF occurring along the bond midway between the 2 atoms. Ionic bonding is indicated by spherical ELF distributions around the atom cores with area along bond length of zero probability. As the degree of covalency increases within the ionic bond, the attractor (maxima) migrates towards the center of the bond and does not completely circumscribe the atomic cores. The relative position of the attractor

indicates the polarity of the chemical bond. Metallic-like bonding is indicated when the ELF is delocalized over a region that is not covered by the cores (i.e., diffusely distributed). Figure 1 shows the total charge density and ELF for the undoped B_6O.

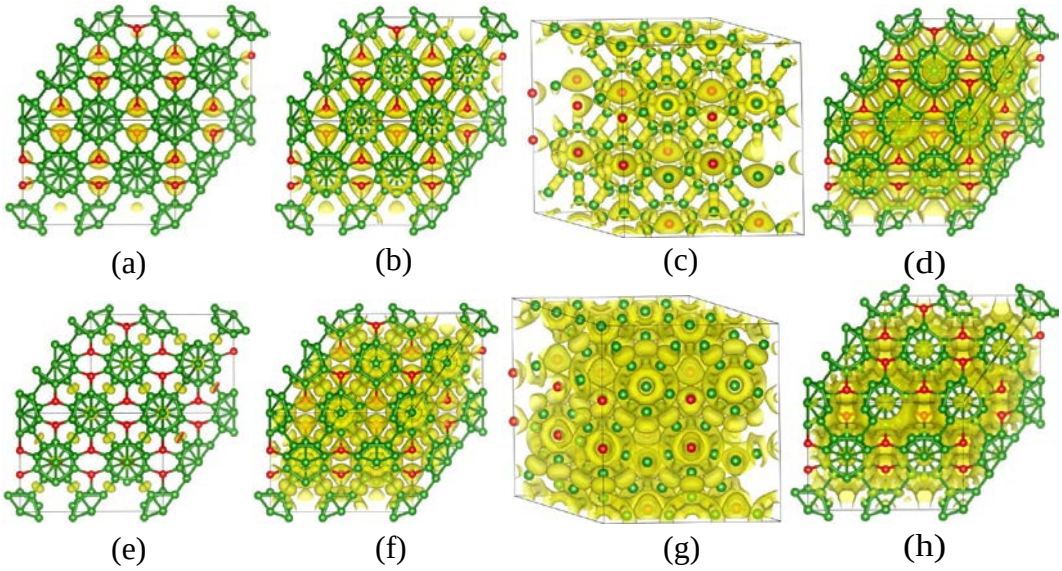

Fig. 1 Total charge density for B_6O at different isovalues: a) 1.2 (15% of max.), b) 0.81 (10% of max.), c) 0.81 (another view), and d) 0.54 (7% of max.). ELF at different isovalues: e) 0.89 (90% of max.), f) 0.7 (70% of max.), g) 0.7 (another view), and h) 0.25 (25% of max.).

As discussed in our previous report,[10] there are several distinct bond types within the B_6O structure: 1) intra-icosahedral bonds (1.78 Å) between boron forming the equator of the icosahedra, 2) intra-icosahedral bonds (1.76 Å) between polar boron at the icosahedra apex, 3) intra-icosahedral bonds (1.78–1.81 Å) between a polar and equatorial boron within the icosahedra, 4) inter-icosahedral bonds (1.7 Å) between 2 polar boron atoms from different icosahedra, and 5) inter-icosahedral bonds (1.5 Å) between equatorial boron and oxygen. The O atoms occupy the interstitial volume between the icosahedra. Each O atom coordinates to 3 equatorial B_e atoms, each from different neighboring icosahedra.

From the charge density, it is clear that the bonding between boron and oxygen atoms is primarily ionic. As illustrated in Fig. 1a, the charge density isosurface at isodensity value equal to 1.2 is localized around the oxygen ions. The B_p –B_p (subscripts p, e, and I are used to represent polar, equatorial, and interstitial sites respectively) inter-icosahedral bonding between boron atoms connecting 2 B_{12} icosahedra are shorter and have stronger covalent character than the bonds connecting boron within the icosahedra. As the charge density isovalue is decreased to 10% of maximum (Fig. 1b), the charge density lobes show highly directional covalent bonding between the B_p –B_p bonds joining the 2 icosahedra.

Also at this isovalue, an isosurface ring joining the 6 equatorial B_e atoms begins to develop (Fig. 1c). The boron atoms within the B_{12} icosahedra are connected to each other by 3 center covalent bonds. As the charge density isovalue decreased further to 7% of the maximum, the isosurface spreads to the entire region around the B_{12} icosahedra creating a "metallic like" surface (Fig. 1d).

Figure 1 also includes the ELF for this system at various isovalues. The ELF value near 0.89 (Fig. 1e) highlights the electron localization along the B_p-B_p bonds between different icosahedra. As already noted, this bond is shorter and consists primarily of a highly directional covalent bond. When the ELF value decreases to 0.7 (Fig. 1f, 1g) the ELF surface encompasses all of the atoms. This ELF surface shows 3 distinct bonding regions (basins): (Region 1) shorter B_p-B_p bonds connecting 2 icosahedra, (Region 2) surrounding O atoms, and (Region 3) surrounding the B_{12} icosahedra. Each region represents a distinct bonding type. Region 1 contains the stronger highly directional covalent bond between 2 B_p atoms in 2 icosahedra. Region 2 includes an ionic bond between an equatorial boron and an oxygen atom whereas region 3 is the intra-atom bonding of boron (B_p, B_e) atoms, which make up the icosahedral frame. As the ELF value is further decreased, the 3 basins merge into each other (Fig. 1h). We performed the Bader[19] charge analysis for this system. The charge transfer from polar B_p atoms is in the range of 0.01–0.09 electrons, emphasizing the covalent nature of the bonds connected with these atoms. For the equatorial B_e atoms, the charge transfer is in the range of 0.45–0.48 electrons. The charge gained by the oxygen atoms is between 1.54 and 1.55 electrons. Each O atom is bonded to 3 B_e atoms from different icosahedra. The charge transfer to the O atom confirms the ionic nature of the B_e-O bond.

It is interesting to note the behavior of the charge density and ELF after carbon doping (see Appendix A). When C is doped at an oxygen site, the sp^2 hybridized carbon forms bonds with 3 neighboring equatorial B_e atoms (B_e-C bond length is 1.52 Å). The resulting B-C-B bond angles are 119.39°, which is nearly equal to the standard 120° bond angle for sp^2 hybridization. The charge density isosurface is evenly distributed around the C-B_e bonds, whereas the ELF shows 3 lobes along 3 C- B_e bonds indicating strong covalent bonding between these atoms. If 2 carbon atoms are doped at 2 neighboring oxygen sites, both carbon atoms become sp^2 hybridized and form bonds with nearest neighboring equatorial boron atoms. When an interstitial is placed between these 2 carbon atoms, forming C-O-C, C-B-C or C-C-C chains, the bonding changes significantly. If the interstitial is either carbon or boron, the 2 terminal carbon atoms become tetrahedrally "sp^3 like" bonded, whereas the interstitial boron or carbon atom are coordinated only to the terminal carbon.

The variation in the bond angles around the carbon atom reflects the changing nature of the bonding. For the C-B-C chain configuration (C_O-B_e and C_O-B_i bond lengths are 1.57 Å and 1.44 Å, respectively), the 3 B_e-C-B_e bond angles are 116.6°, whereas the B_e-C-B_i bond angles are 100.75°. For the C-C-C chain configuration (C_O-C_i and B_e-C_O bonds distances are 1.32 Å and 1.61 Å, respectively), the 3 B_e-C_O-B_e bond angles are 114.49°, whereas the B_e-C_O-C_i bond angles are 103.82º. This indicates that the C-C bond is stronger than the B_e-C bond. Also, the B_e-C bonds weaken for C-C-C chain when compared with the C-B-C chain. This is reflected in the larger B_e-C bond distances in C-C-C chain (1.61 Å) when compared with the C-B-C chain (1.57 Å). Both the B-C-B and C-C-C chain remain linear. However, the C-O-C chain is slightly bent with the angle 150.14°. The other B_e-C-B_e angles for the C-O-C chain configuration are in the range of 108.4°–116.8°. For the carbon-doped B_6O system, the carbon hybridization bond angles are very different from the standard sp^2 (120°) and sp^3 (109.4°) hybridization bond angles, indicating a higher degree of bonding complexity. When one equatorial boron atom neighboring a C-B-C chain is replaced by carbon, a C_e-C_O bond forms between the equatorial carbon and C-B-C chain. The B_e-C_e-B_e bond angle for this C is 110.64°, where as the C_e-C_O-B_e bond angles are 118.90°. For the other carbon atom in the chain the B_e-C_O-B_e bond angles are 115.63°–116.52°. If instead, the carbon atom replaces a polar boron neighboring a C-B-C chain (C_p-CBC), the B_e-C-B_e bond angles are in the range of 115.31°–116.87° for one C-atom in the C-B-C chain and 115.76°–116.86° for other C atom.

To understand the charge transfer in the doped systems, we calculated the charge density difference by subtracting the charge density of the isolated C-B-C or C-C-C chains from the total charge density of the combined system. The excess and depletion charge densities for this system indicate that charge is transferred from the B_{12} icosahedra to the carbon atoms in the chain. For the C-B-C chain configuration, the central boron atom also transfers charge to the 2 carbon atoms in the chain. However, for the C-C-C chain configuration, there is charge transfer from the 2 terminal carbon atoms to the interstitial C atom.

The total DOS (see Fig. 2 and Appendix B) gives further information about the nature of bonding in the undoped and carbon-doped B_6O systems. Our results indicate that B_6O is a semiconductor with the calculated band gap of approximately 2.6 eV. The band gap is slightly higher than that of previous reported value of 2.4 eV.[20,21] Density functional theory (DFT) is known to underestimate the band gaps. The band gap reported for B_6O based on many body perturbation theory is 3 eV[22], whereas density functional tight binding theory (DF-TBT) calculates a 3.45 eV band gap.[23] For the pure B_6O, the states near the higher

energy part of the valence band are mainly boron 2p states, followed by oxygen 2p and boron 2s states in the middle and lower energy range. The lower end of the conduction band contains empty boron 2p states.

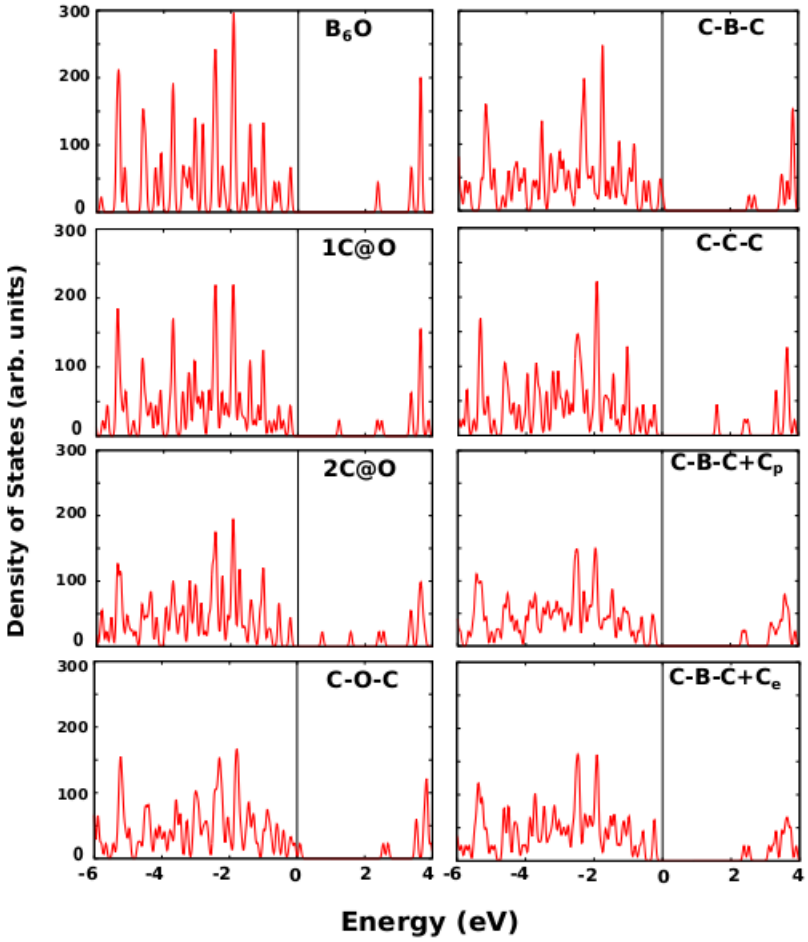

Fig. 2 Schematic representation of total DOS for pure and doped B_6O

Appendix B contains the total and atom resolved partial density of states for carbon substituting for different sites within the B_6O unit cell. When one oxygen atom is replaced by carbon, a new peak appears 1.2 eV above the Fermi level. This peak has a significant contribution from the empty 2p orbitals of the carbon atom. When a second carbon atom is doped at the neighboring oxygen, the DOS shows significant variations in the lower energy part of the conduction band. There are also some delocalized states near the Fermi level. The empty 2p levels of each C_O atom split into slightly lower (0.71 eV) and higher energy states (1.56 eV) than the 1.2 eV peak present when only a single oxygen is substituted by carbon. For the C-B-C chain configuration, no such peak is observed. For the C-B-C configuration, a new peak is created at the Fermi level with contributions from 2p orbitals of the carbon and boron atoms in the C-B-C chain. For the C-C-C

chain configuration, the DOS shows a peak at 1.55 eV above the Fermi level. This peak is dominated by the 2p states of the interstitial carbon atom. When an additional carbon atom is doped in the C-B-C doped configuration, the DOS shifts slightly towards the lower energy range. This shifting of DOS towards the lower energy is an indication of the improved stability of the C_p-CBC and C_e-CBC systems.

3.2 Structural and Elastic Properties

The finite strain method is the most common method to compute the stiffness coefficients of materials. In this approach, the ground state structure is strained according to symmetry dependent strain patterns with varying amplitudes. The stress tensor is determined after a reoptimization of the internal structure parameters. The elastic stiffness coefficients follow from Hooke's law[24,25] as the proportionality coefficients relating the applied strain to the computed stress.

$$\sigma_i = \sum_{i,j=1}^{6} c_{ij}\varepsilon_j \ . \tag{1}$$

Equation 1 consists of a set of 6 linear equations with 27 variables: 6 components of stress and 21 elastic constants. The elastic behavior of a completely asymmetric material (triclinic) is specified by 21 independent elastic constants, whereas an isotropic material (cubic) requires only 3. In between these limits, the necessary number is determined by the symmetry of the material. For a hexagonal crystal, there are 6 unique symmetry elements c_{11}, c_{12}, c_{13}, c_{33}, c_{44}, and c_{66}. However, since $c_{66}= (c_{11}-c_{12})/2$, there are only 5 truly independent symmetry elements. In Table 1, we compared the calculated lattice parameters and elastic constants for undoped B_6O with the earlier results from the scientific literature.

Table 1 Summary of the calculated B_6O lattice parameters (Å) and single crystal elastic constants C_{ij} (GPa) with previously reported values

Property	PAW-GGA[20]	PAW-LDA[26]	GGA[27]	LDA[28]	Our Calculations	
					1×1×1	2×2×1
a	5.391	5.328	5.331	5.127	5.392	10.792
c	12.312	12.147	12.124	. . .	12.327	12.312
c_{11}	603	615	614.99	586.88	585.70	586.05
c_{33}	459	474	474.12	443.87	458.99	466.06
c_{12}	109	140	122.22	133.19	128.18	121.66
c_{13}	50	61	46.51	47.41	53.30	45.29
c_{44}	179	180	192.38	. . .	176.87	178.38
c_{14}	. . .	. . .	. . .	22.75	22.4	22.25

The bulk modulus B and shear modulus G can be measured to determine elastic properties of materials. On the basis of the scheme of Voigt[29] (assuming uniform strain) and Reuss,[30] (assuming uniform stress) and with the approximation of Hill's[31] arithmetic average, we calculated the bulk modulus B and shear modulus G for B_6O. Tables 2, 3, and 4 compare the calculated lattice parameters, elastic constants, and elastic moduli for the pure and doped B_6O systems. Furthermore, the Young modulus E and Poisson's ratio α have been calculated from the following equations for the isotropic material:

$$\mathrm{E} = \frac{9BG}{(3B+G)}, \alpha = \frac{(3B-2G)}{2(3B+G)}. \quad (2)$$

Table 2 Calculated lattice parameters (Å), cell volume (Å^3) and single crystal elastic constants C_{ij} (GPa) for pure and carbon-doped B_6O

Property	B_6O	C@B_p	C@O	2C@O	C-B-C	C-C-C	C-B-C + C_p
a	10.792	10.791	10.806	10.819	10.833	10.832	10.825
c	12.312	12.307	12.307	12.307	10.833	12.302	12.297
V	1,241.94	1,241.29	1,244.56	1,247.65	1,250.82	1,250.04	1,248.28
C_{11}	586.05	578.21	582.24	583.07	581.6	579.1	585.1
C_{33}	466.06	459.2	460.89	466.73	472.3	469.6	472.1
C_{12}	121.66	121.68	117.52	119.38	120.1	120.8	122.1
C_{13}	45.29	44.54	42.04	48.94	51.6	49.4	51.4
C_{44}	178.38	177.92	176.43	172.56	171.6	173.5	176.0
C_{14}	22.25	20.25	19.87	19.35	15.9	21.0	21.6

Table 3 Calculated lattice parameters and elastic constants C_{ij} (GPa) for B_6O with 2 C atoms substituting for neighboring O, separated by O interstitial (C_O-O_i-C_O chain)

a	b	c	C_{11}	C_{12}	C_{13}	C_{14}	C_{15}
10.810	10.834	12.316	540.88	79.98	8.32	3.94	5.78
C_{16}	C_{22}	C_{23}	C_{24}	C_{25}	C_{26}	C_{33}	C_{34}
4.27	530.25	5.14	4.84	24.68	5.58	410.57	5.7
C_{35}	C_{36}	C_{44}	C_{45}	C_{46}	C_{55}	C_{56}	C_{66}
7.30	5.78	210.57	0.89	44.93	180.38	0.96	126.38

Table 4 Comparison of the calculated elastic moduli (V-Voight, R-Reuss, H-Hill) in GPa, Poison's ratio, and polycrystalline elastic anisotropyVoight Reuss (AVR)

Property	B_6O	C@B_p	C@O	2C@O	C_O-O_i-C_O	C-B-C	C-C-C	C-B-C + C_p
B_V	229.19	226.35	225.40	229.71	185.39	231.38	229.65	232.45
G_V	212.84	210.48	211.96	209.77	196.01	208.93	209.13	211.2
B_R	223.31	220.41	219.47	224.33	178.12	226.5	224.6	227.27
G_R	205.86	204.2	205.11	202.64	177.94	202.35	202.12	204.28
B_H	226.25	223.38	222.43	227.02	181.76	228.94	227.12	229.86
G_H	209.35	207.34	208.54	206.21	186.98	205.64	205.62	207.74
E_H	480.01	475.05	476.65	474.85	417.7	474.77	473.87	478.94
α_H	0.15	0.15	0.14	0.15	0.12	0.15	0.15	0.15
AVR (%)	1.668	1.513	1.642	1.727	4.831	1.601	1.704	1.666

To the best of our knowledge, there are few experimental studies of the elastic constants for B_6O. Petrak et al.[32] used the resonant-sphere technique to obtain the aggregate elastic moduli for hot-pressed B_6O specimens under ambient conditions. He reported the bulk modulus B, shear modulus G, and Young's modulus E as 230, 206, and 472 GPa, respectively, whereas Andrievskiy[33] reported 228, 204, and 471.4 GPa, respectively. Earlier ab initio studies report that the bulk moduli (B) for B_6O vary from 222 to 235 GPa.[34–37] Our calculated value of B_H = 226.25 GPa agrees with the previous studies. Our calculated bulk modulus, shear modulus, and Young's modulus are also in agreement with the experimental findings.[33,34]

Carbon doping significantly changes both the elastic constants and elastic moduli. The doping of one carbon atom at a boron or oxygen site decreases the elastic moduli between 0.4% and 1.7%. The doping of 2 carbon atoms at 2 oxygen sites increases the bulk modulus by 0.3%, yet decreases the shear and Young's modulus by 0.5%. When there is an additional interstitial oxygen between the 2 C_O, the elastic moduli are significantly decreased. For this case, the bulk modulus

decreases by 20%, whereas the shear and Young's moduli decrease by 10%–13%. It is interesting to note the change in the elastic moduli for C-B-C and C-C-C local chain configurations within B_6O. When either a boron or carbon atom is doped as the interstitial between 2 C_O, the bulk modulus increases, whereas the shear modulus and Young's moduli decrease. The C-B-C chain configuration has higher B, G, and Y moduli than the C-C-C chain configuration. If an additional carbon is doped in either a polar or equatorial sites of a icosahedra neighboring a C-B-C chain, further improvements in the 3 moduli can be seen. However, the G and Y values are lower than that of the undoped B_6O.

4. Conclusions

In summary, we calculated the structural and elastic properties of pure and carbon-doped B_6O under ambient conditions within the plane-wave pseudopotential DFT. We demonstrate how carbon doping can be used to modify the electronic structure and elastic properties of the hexagonal B_6O. It is energetically preferable for carbon to replace oxygen rather than boron. When carbon replaces oxygen, the lattice parameters and cell volume expand to relieve the residual stress. The energetic cost of carbon doping increases when 2 carbon atoms replace 2 oxygen atoms. Adding an interstitial oxygen along a C_O-C_O chain significantly changes the B_6O unit cell and decreases the elastic moduli leading to a reduction in material hardness. In contrast, interstitial boron or carbon doping leading to local C-B-C or C-C-C chain configurations improves the bulk modulus at the expense of the shear and Young's modulus. The C-B-C chain configuration results in higher B, G, and Y moduli than the C-C-C chain configuration. The 3 moduli further improve as additional carbon atoms are substituted for boron in either the polar or equatorial site of a neighboring B_{12} icosahedra. These calculations suggest that doping can either harden or soften B_6O. The hardening or softening depends on the location and the type of a dopant. When the doping creates a B_4C-like local structure within B_6O, there is an increase in the bulk modulus and decrease in shear and Young's moduli. This study demonstrates that the B_4C-like local doping could be used to improve the mechanical stability and elastic properties of B_6O.

5. References

1. He D, Zhao Y, Daemen L, Qian J, Shen TD. Boron suboxide: as hard as cubic boron nitride. Appl. Phys. Lett. 2002;81:643.

2. Machaka R, Derry TE, Sigalas I. Nanoindentation hardness of hot-pressed boron suboxide. Materials Science and Engineering. 2011;A528:5778.

3. He D, Shieh SR, Duffy TS. Strength and equation of state of boron suboxide from radial x-ray diffraction in a diamond cell under non-hydrostatic compression. Phys. Rev. B. 2004;70:184121.

4. Herrmann M, Thiele M, Jaenicke-Roessler K, Freemantle CS, Sigalas I. Oxidation resistance of B_6O-materials with different additives. J. Eur. Ceram. Soc. 2011;31:1771.

5. Bush PR. On the toughening mechanisms present in boron suboxide materials with sintering aids. [master's dissertation]. [Johannesburg (South Africa)]: University of Witwatersrand; 2011.

6. Andrews AA. Development of boron suboxide composites with improved toughness. [PhD thesis]. [Johannesburg (South Africa)]: University of Witwatersrand; 2008.

7. Reddy KM, Hirata A, Liu P, Fujita T, Goto T, Chen MW. Shear amorphization of boron suboxide. Scripta Materialia. 2014;76:9.

8. Wang Z, Zhao Y. In situ pressure Raman spectroscopy and mechanical stability of superhard boron suboxide. Appl Phys Lett. 2005;86:041911.

9. Nifise E. Study of sintering and structure property relationships in boron suboxide – alkaline earth metal oxide, cobalt, and nickel compound. [master's dissertation]. [Johannesburg (South Africa)]: University of Witwatersrand; 2009.

10. Rahane AB, Dunn JS, Kumar V. First principles atomistic model for carbon doped boron suboxide. Aberdeen Proving Ground (MD): Army Research Laboratory (US); 2014 Sep. Report No.: ARL-TR-7106. Also available at http://www.arl.army.mil/www/default.cfm?technical_report=7216.

11. Perdew JP, Burke K, Ernzerhof M. Generalized gradient approximation made simple. Phys Rev Lett. 1996;77:3865.

12. Blochl PE. Projector augmented-wave method. Phys Rev B. 1994;50:17953.

13. Kresse G, Joubert D. From ultrasoft pseudopotentials to the projector augmented-wave method. Phys Rev B. 1999;59:1758.

14. Kresse G, Furthmuller J. Efficient iterative schemes for ab initio total-energy calculations using a plane-wave basis set. Phys Rev B. 1996;54:11169.

15. Vienna Ab Initio Simulation Package (VASP). Vienna (Austria): Technische Universitat Wien, 1999 [Accessed 2014 Sep 1]. https://www.vasp.at/.

16. Higashi I, Kobayashi M, Bernhard J, Brodhag C, Thevenot F. Crystal structure of B_6O. AIP Conf. Proc. 1993;231:201.

17. Hubert H, Garvie LA, Devouard B, Buseck PR, Petuskey WT, McMillan PF. High-pressure, high-temperature synthesis and characterization of boron suboxide (B_6O). Chem Mater. 1998;10:1530.

18. Becke A, Edgecombe K. A simple measure of electron localization in atomic and molecular systems. J. Chem. Phys. 1990;92:5397.

19. Tang W, Sanville E, Henkelman G. A grid-based Bader analysis algorithm without lattice bias. J. Phys. Condens. Matter. 2009;21:084204.

20. Zhang RF, Lin ZJ, Zhao YS, Veprek S. Superhard materials with low elastic moduli: three dimensional covalent bonding as the origin of superhardness in B_6O. Phys. Rev. B 2011;83:092101.

21. Li D, Ching WY. Electronic structure and optical properties of $B_{12}O_2$ crystal. Phys. Rev. B 1996;54:1451.

22. Hautier G, Miglio A, Ceder G, Rignanese GM, Gonze X. Identification and design principles of low hole effective mass p-type transparent conducting oxides. Nature Comm. 2013;4:2292.

23. Enyashin AN, Ivanovskii AL. Structural, elastic, and electronic properties of icosahedral boron subcarbides ($B_{12}C_3$, $B_{13}C_2$), subnitride $B_{12}N_2$, and suboxide $B_{12}O_2$ from data of SCC-DFTB calculations. Phys. Solid State. 2011;53:1569.

24. Ashcroft NW, Mermin ND. Solid state physics. Philadelphia (PA): Saunders; 1976.

25. Nye JF. Physical properties of crystals. Oxford (UK): Clarendon; 1957.

26. Letsoalo TE, Lowther JE. Computational investigation of elastic properties of bulk and defective ultrahard B_6O. J. Superhard Mater. 2011;33:19.

27. Lu YP, He DW. Structure and elastic properties of boron suboxide at 240 GPa. J. Appl. Phys. 2009;105:083540.

28. Lee S, Bylander DM, Kleinman L. Elastic moduli of B_{12} and its compounds. Phys. Rev. B. 1992-I;45:3245.

29. Voigt W. Lehrbush der kristallphysik. Leipzig (Germany): Taubner;1928.

30. Reuss A, Angew Z. Berechung der fliessgrenze von mischkristallen. Math. Mech. 1929;9:55.

31. Hill R. Elastic behaviour of a crystalline aggregate. Proc. Phys. Soc. A. 1952;65:349.

32. Petrak DR, Ruh R, Atkins GR. Mechanical properties of hot pressed boron suboxide and boron. Am. Ceram. Soc. Bull. 1974;83:569.

33. Andrievskiy RA. New superhard nanomaterials-based high-melting point compounds. Proceedings of the 17th International Offshore and Polar Engineers Conference; 2007 Jul 1–6; Lisbon, Portugal. Cupertino (CA): International Society of Offshore and Polar Engineers; c2007. p. 2875.

34. Zhao Y, He D, Qian J, Zhang J. Synthesis and characterization of nano-composite superhard materials. Mater. Res. Soc. Symp. Proc. 2006;987:0987-PP01-11.

INTENTIONALLY LEFT BLANK.

Appendix A. Electron Localization Function for Pristine and Carbon-Doped B_6O

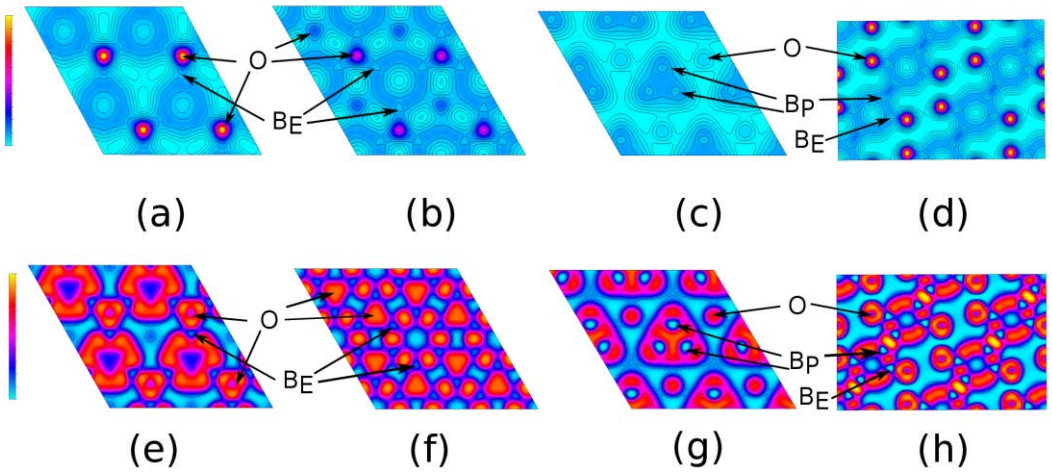

Fig. A-1 Two-dimensional (2-D) plots for total charge density (a–d) and electron localization function (ELF) (e–h) for the B_6O. The plane normal to [001] direction: a–c and e–g; the plane normal to [110] direction: d and h.

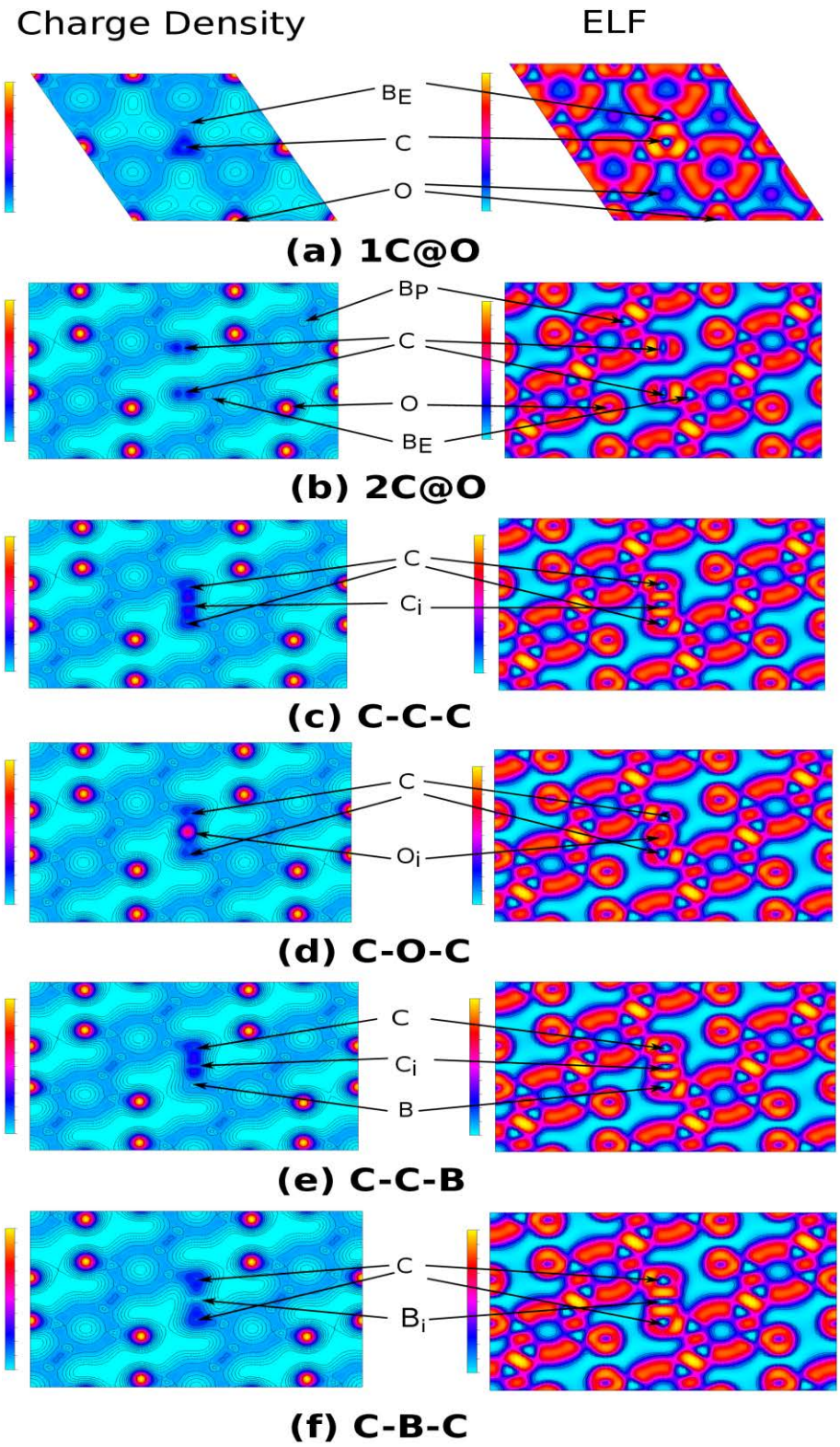

Fig. A-2 2-D plots for the total charge density and ELF for C-doped B_6O case: a) the plane normal to [001] direction; b) and f) the plane normal to [110] direction.

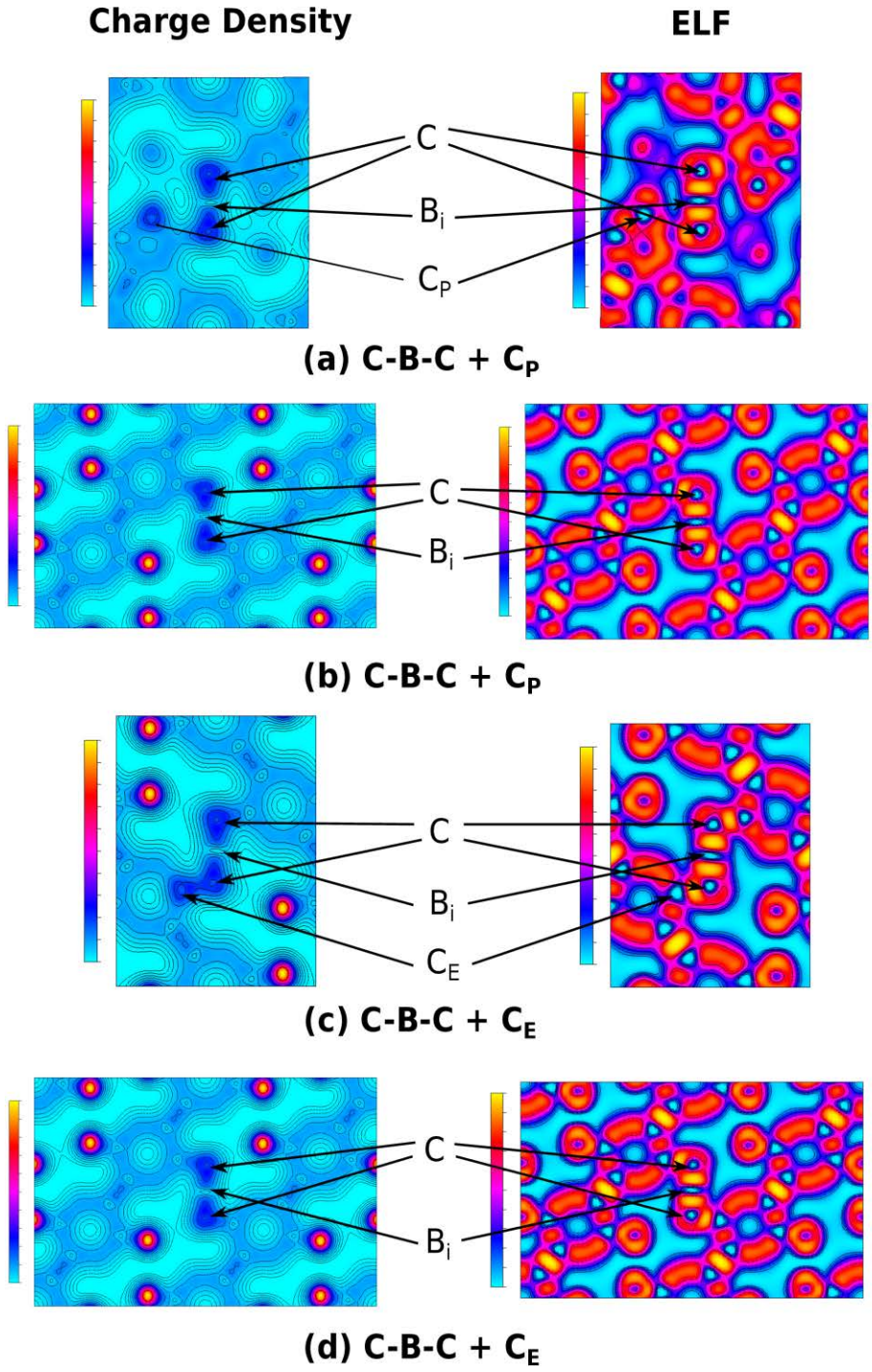

Fig. A-3 2-D plots for the total charge density and ELF for C- doped B_6O case. a) represents the plane containing doped C-B-C atoms and C_P atom; b) represents the plane normal to [110] direction; 3c) represents the plane containing doped C-B-C atoms and C_E atom; 3d represents the plane normal to [110] direction.

Appendix B. Atoms Resolved Density of States for Pristine and Carbon-Doped B_6O

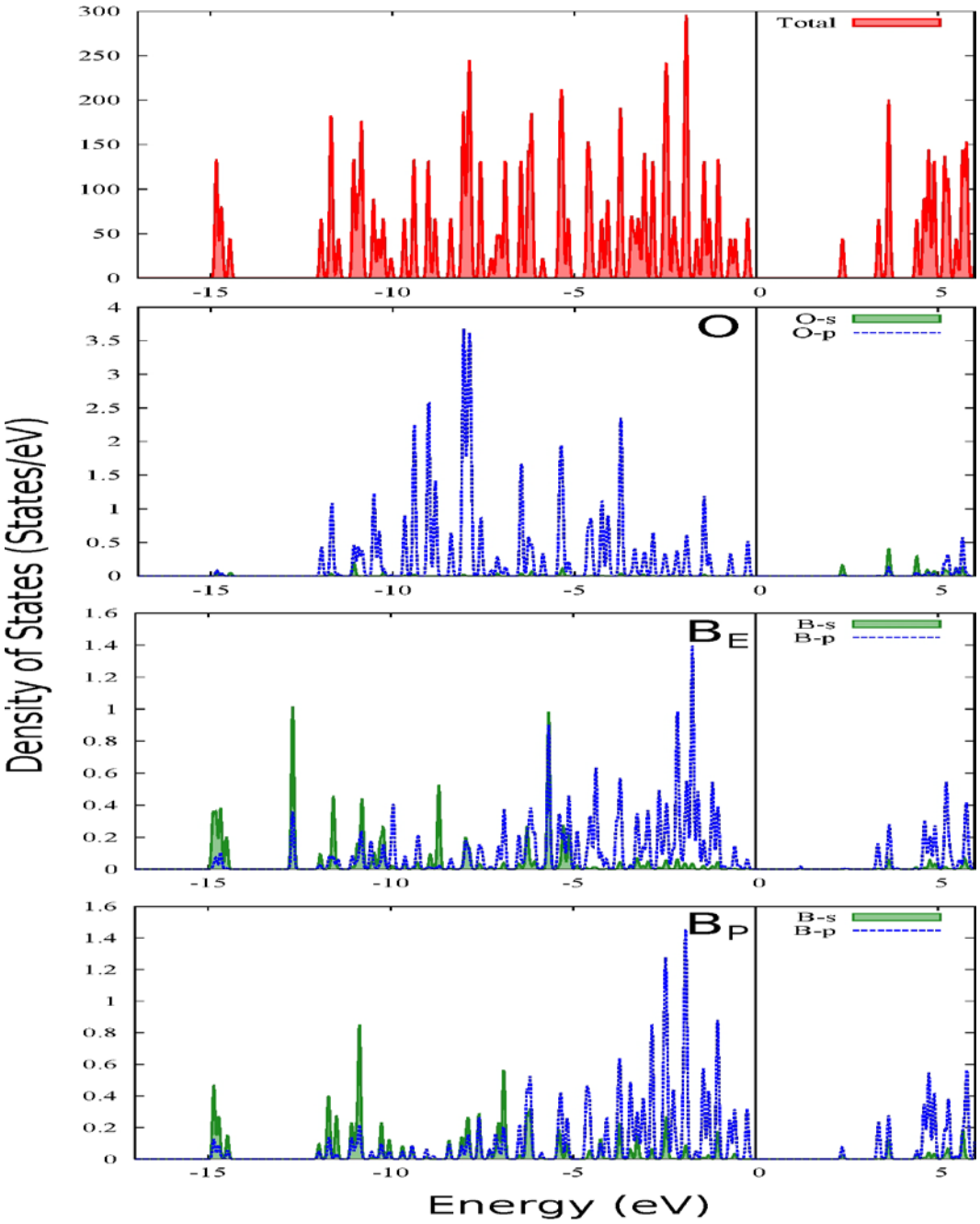

Fig. B-1 Total density of states (TDOS) and atom resolved (O, B_e, and B_p) partial density of states (PDOS) for B_6O

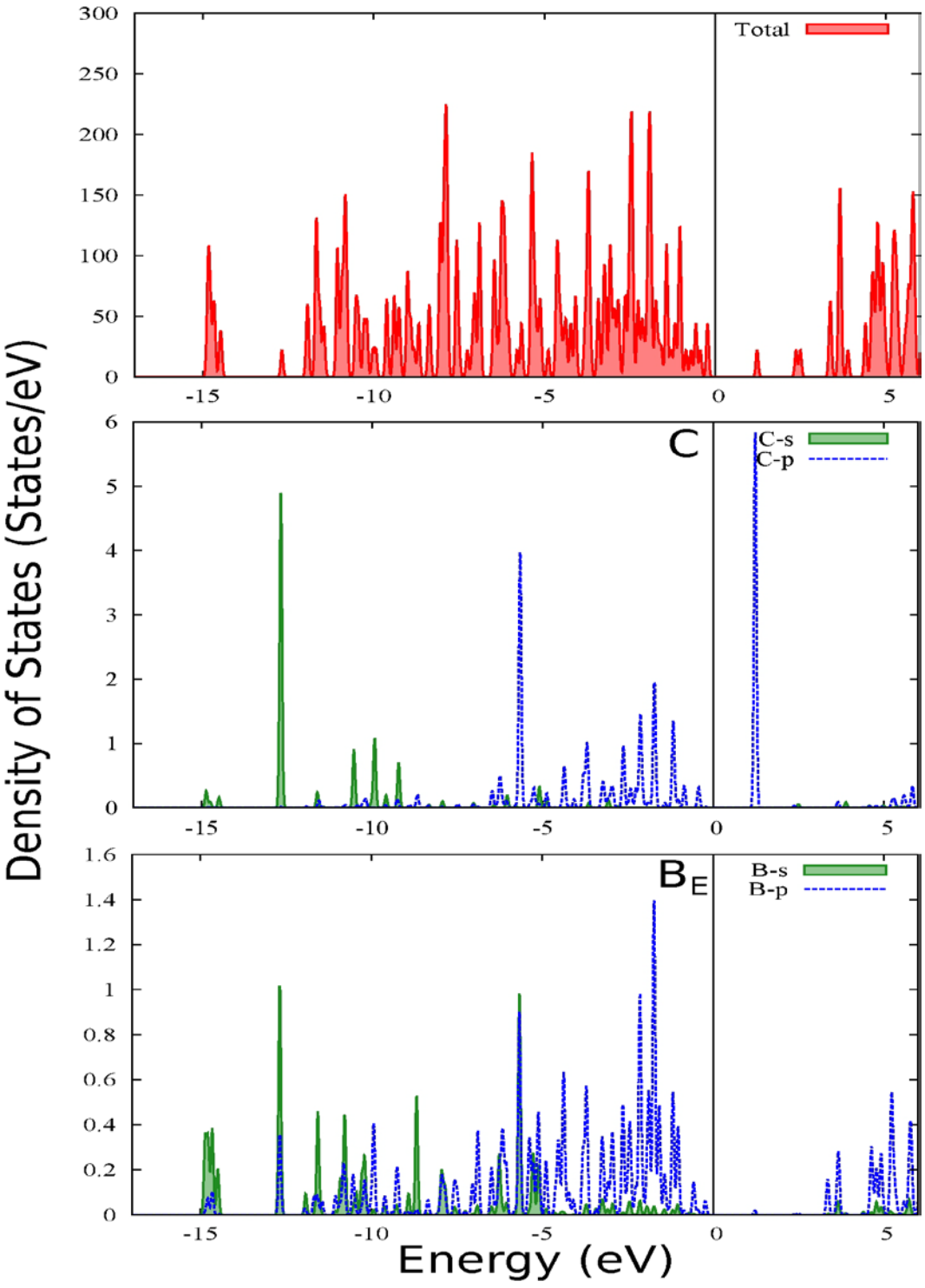

Fig. B-2 TDOS and atom resolved (C_O, nearest B_e) PDOS for B_6O with one C-atom substituted for O

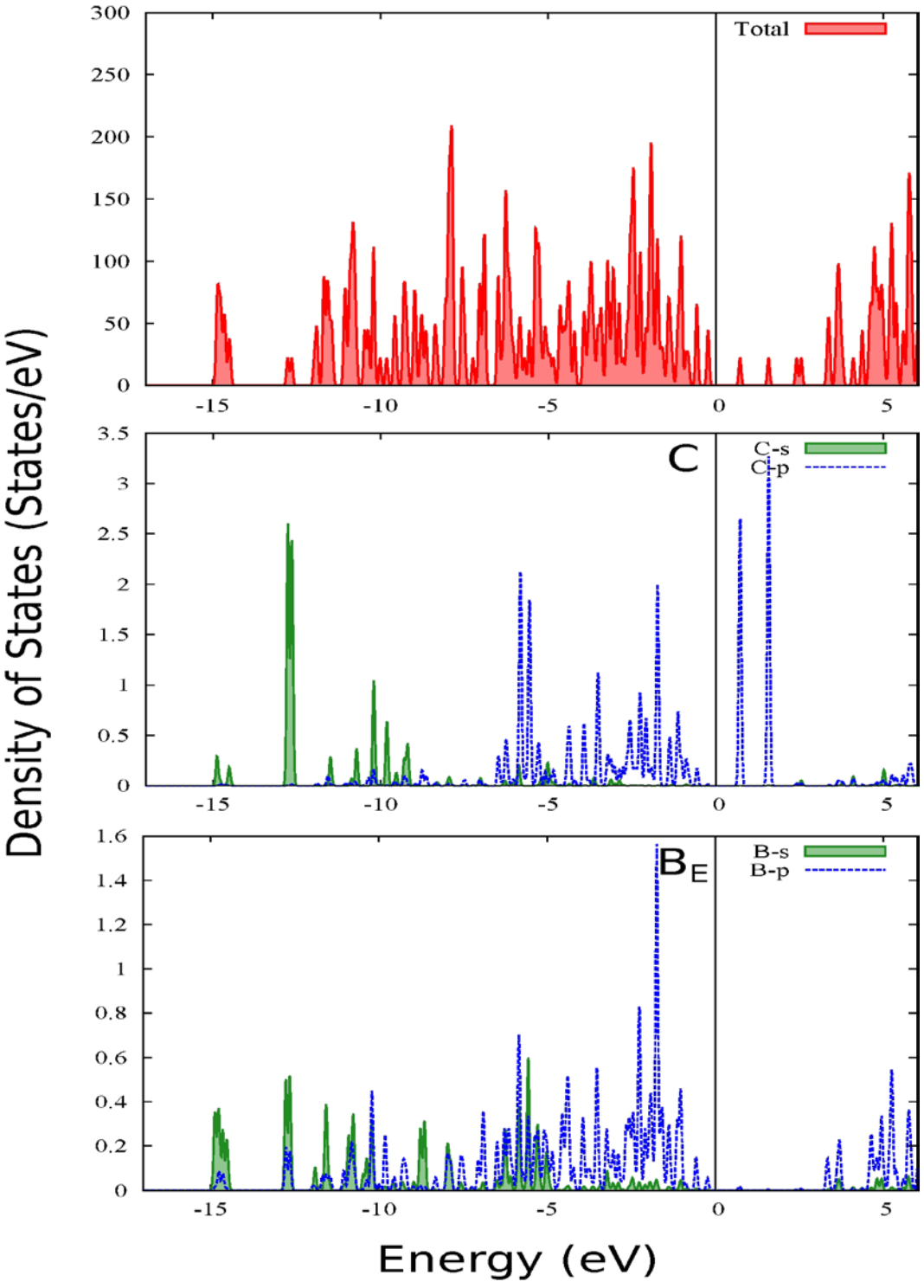

Fig. B-3 TDOS and atom resolved (C_O, nearest B_e) PDOS for B_6O with 2 C substituted for neighboring O. Both C_O have similar PDOS.

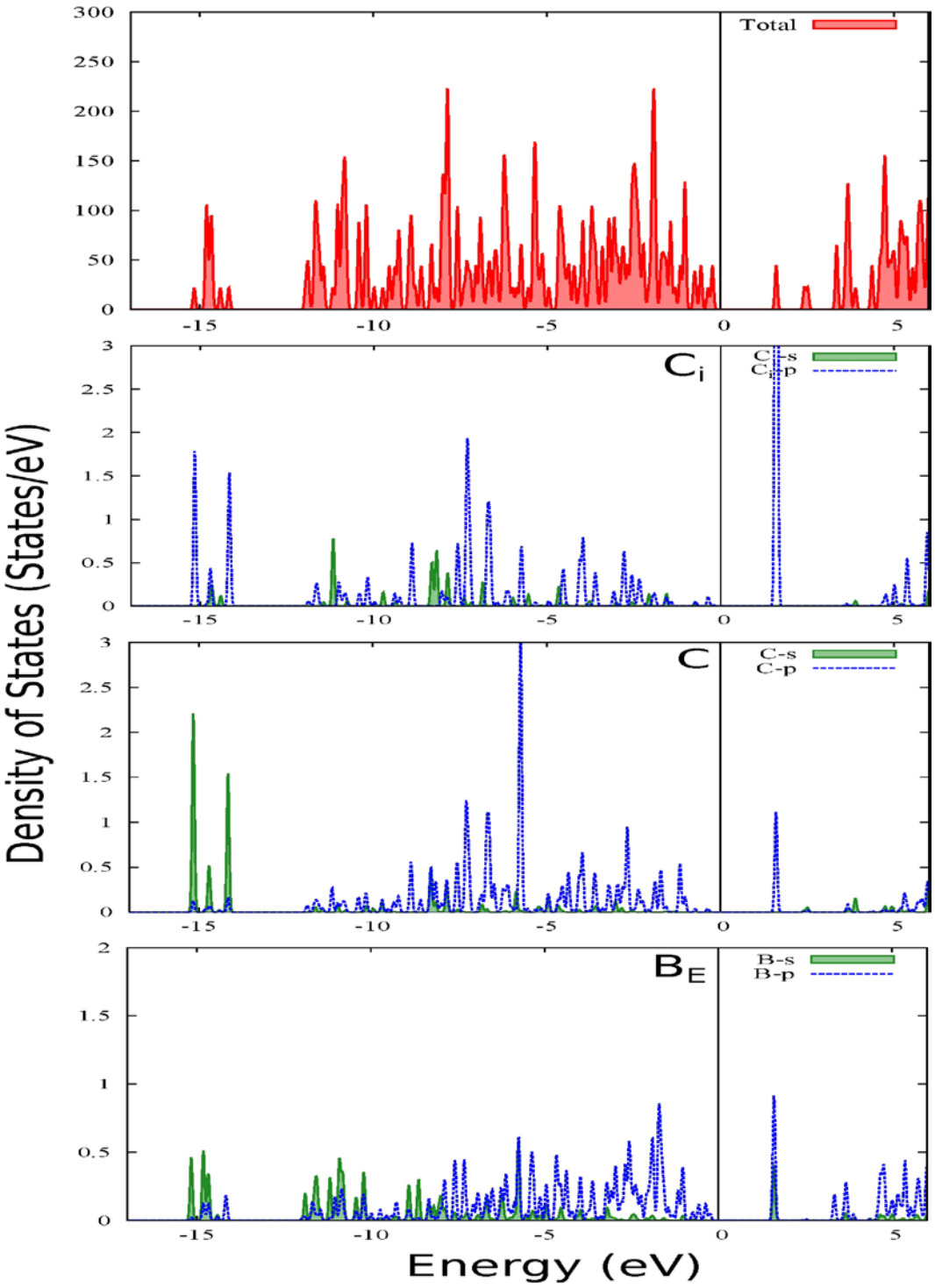

Fig. B-4 TDOS and atom resolved (C_O, O_i, nearest B_e) PDOS for C-O-C chain substitution within B_6O. Both C_O have similar PDOS.

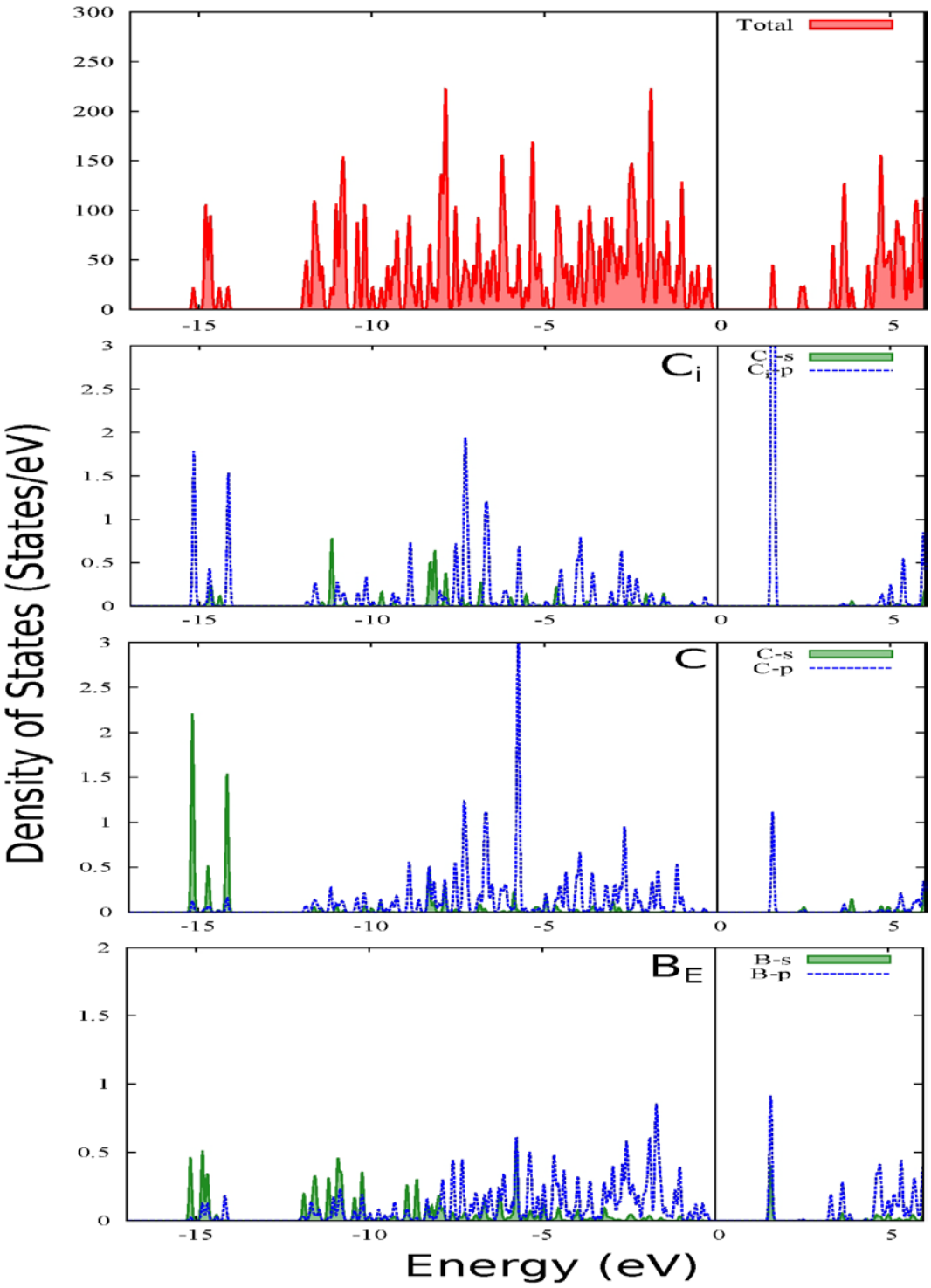

Fig. B-5 TDOS and atom resolved (C_O, C_i, nearest B_e) PDOS for C-C-C chain substitution within B_6O. Both C_O have similar PDOS.

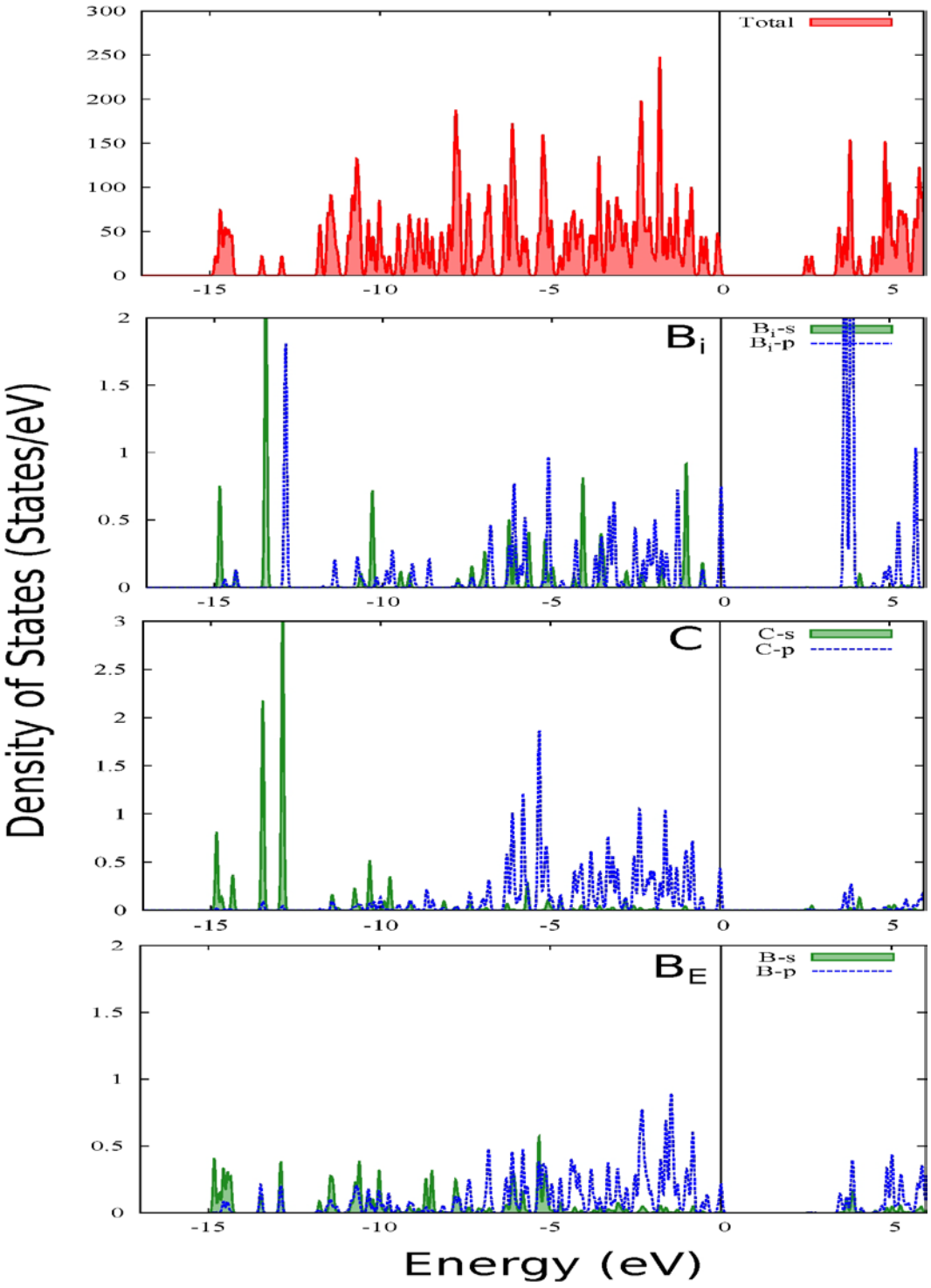

Fig. B-6 TDOS and atom resolved (C_O, B_i, nearest B_e) PDOS for C-B-C chain substitution within B_6O. Both C_O have similar PDOS.

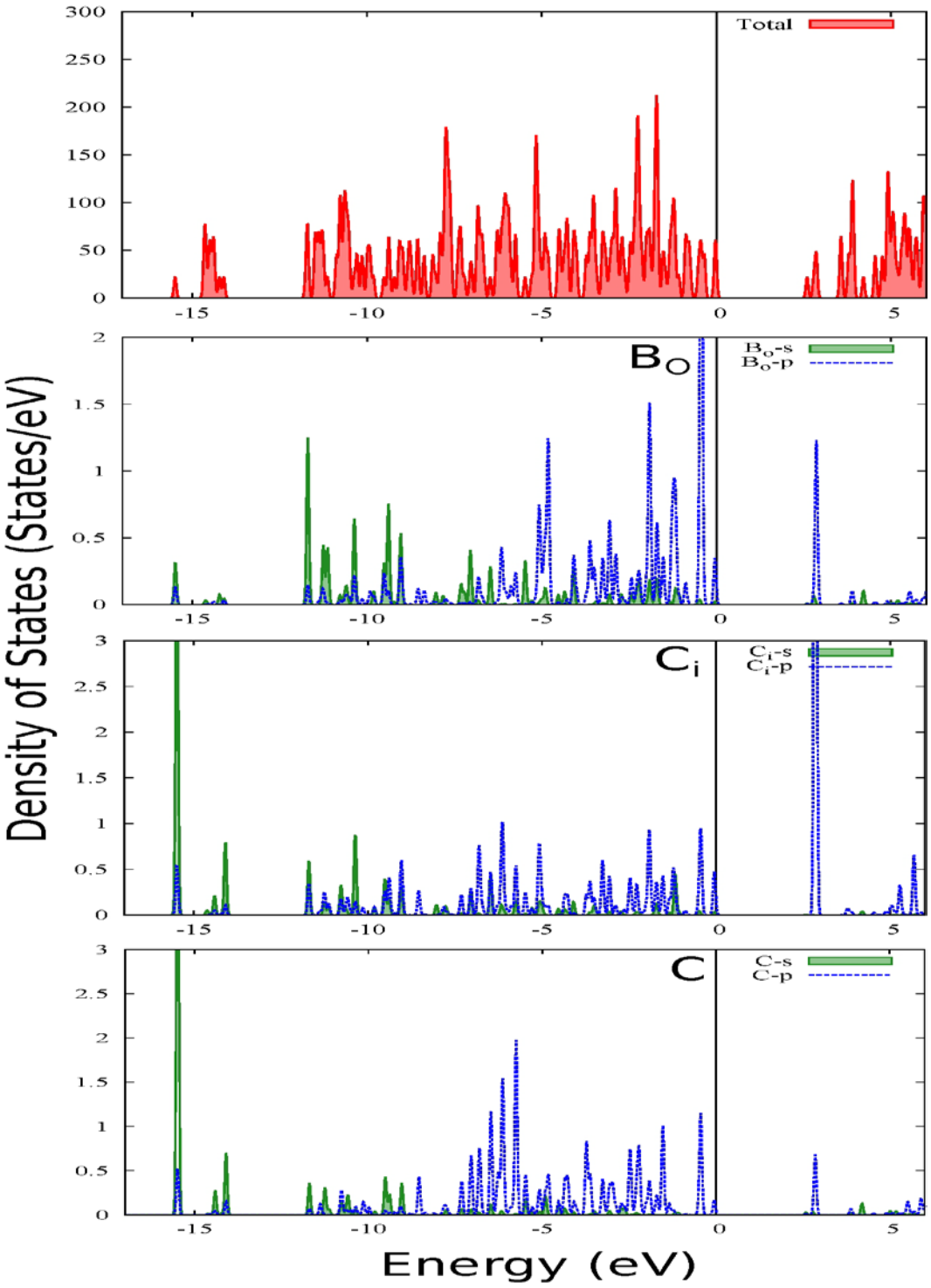

Fig. B-7 TDOS and atom resolved (C_O, B_O, C_i) PDOS for C-C-B chain substitution within B_6O

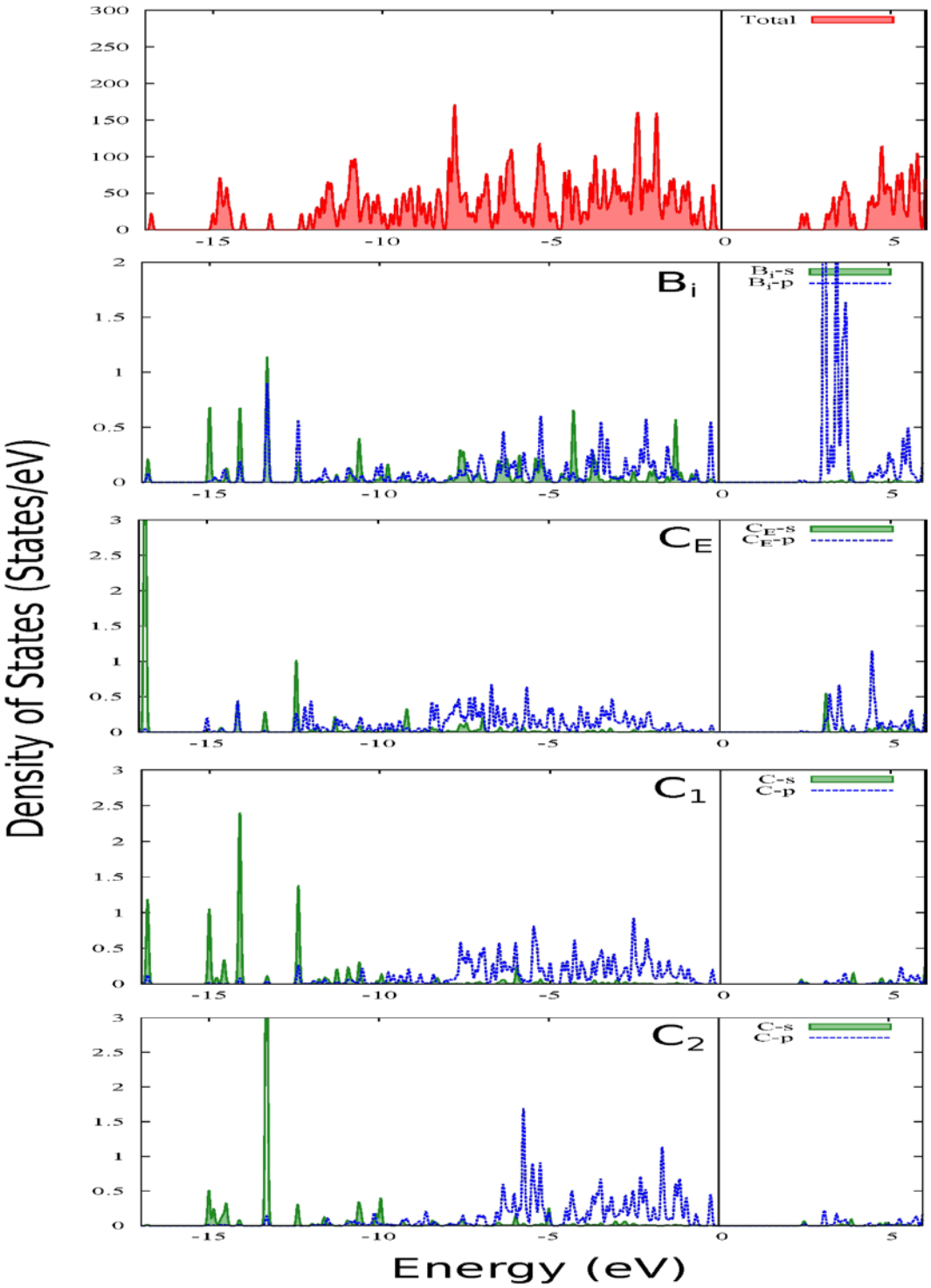

Fig. B-8 TDOS and atom resolved (C_O, B_i, C_e) PDOS for C_e + C-B-C chain substitution within B_6O. C1 is bonded to C_e, C2 is bonded to B_e.

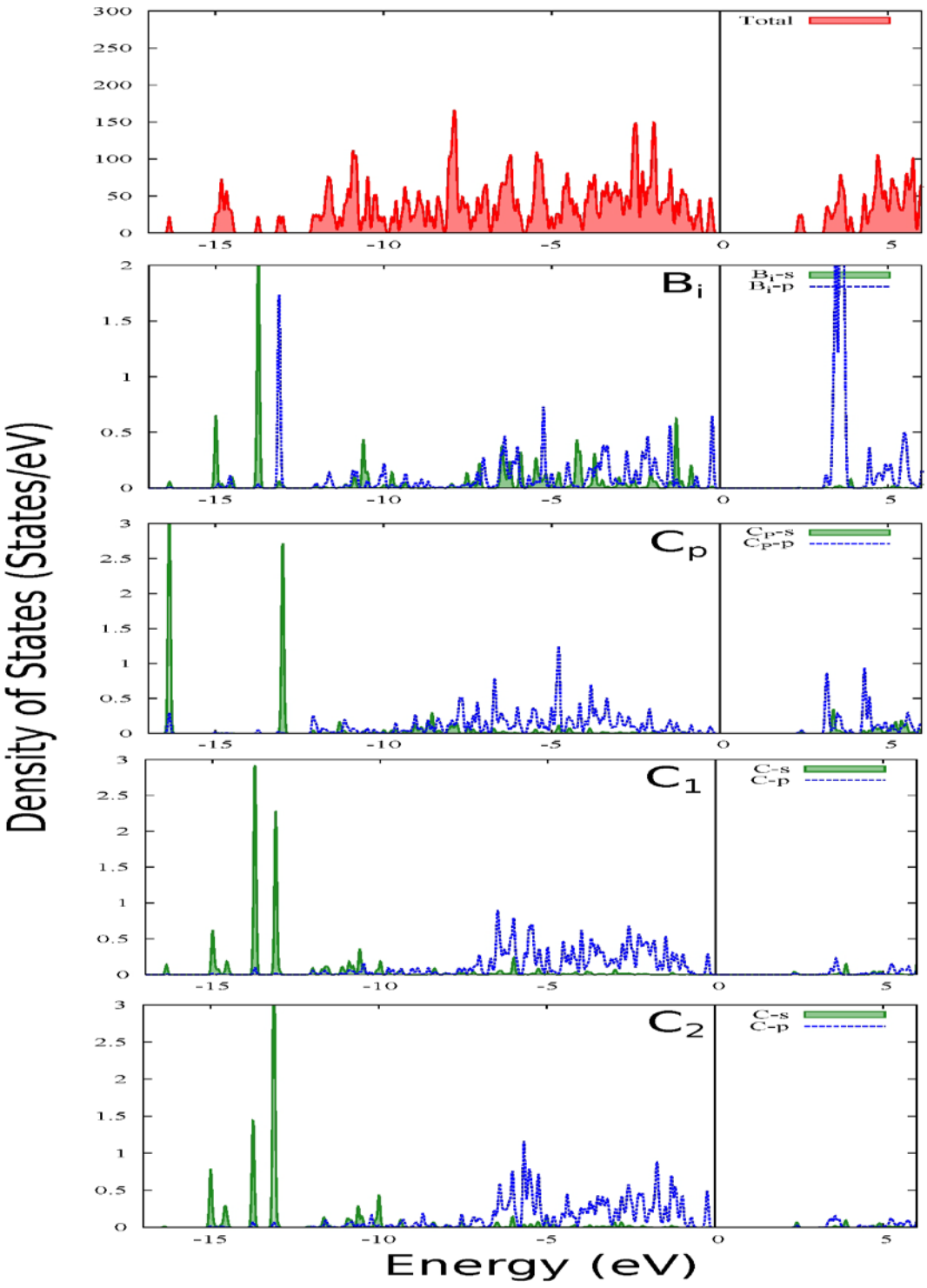

Fig. B-9 TDOS and atom resolved (C_O, B_i, Cp) PDOS for Cp_e + C-B-C chain substitution within B_6O. C1 is separated from C_p by $1B_e$, C2 is bonded to B_e.

List of Symbols, Abbreviations, and Acronyms

AVR	anisotropy Voight Reuss
DOS	density of states
DF-TBT	density functional tight binding theory
DFT	Density functional theory
ELF	electron localization function
GGA	generalized gradient approximation
TDOS	total density of states
PAW	projector augmented wave
PDOS	partial density of states
VASP	Vienna Ab initio Simulation Package

1 (PDF)	DEFENSE TECHNICAL INFORMATION CTR DTIC OCA
2 (PDF)	DIRECTOR US ARMY RESEARCH LAB RDRL CIO LL IMAL HRA MAIL & RECORDS MGMT
1 (PDF)	GOVT PRINTG OFC A MALHOTRA
1 (PDF)	DIR USARL RDRL WMM E J S DUNN